

Generalized stability of a shear flow with a free surface with respect to three-dimensional perturbations

Christos Mallios and Nikolaos A. Bakas*

Laboratory of Meteorology, Department of Physics, University of Ioannina, Ioannina 45110, Greece

(Received 10 July 2016; published 6 February 2017)

Modal and nonmodal growth of three-dimensional perturbations in a shear flow with a free surface are examined for a wide range of Froude numbers. By approximating the mean flow with a piecewise linear profile, the modal instabilities are shown to arise from the interaction of three-dimensional edge waves supported at the interfaces of density discontinuity at the surface and mean vorticity discontinuity at the edges of the shear layer. The mechanism and properties of the instability are explained in terms of the dynamics of the edge-wave interactions. Previously reported modal stability analysis restricted to two-dimensional perturbations in the plane of the flow accurately predicts the fastest growing perturbations but underestimates the range of length scales for the unstable structures. Robust nonmodal transient growth of perturbations within a few advective time units is found. For low Froude numbers or low values of the shear, three-dimensional perturbations with small horizontal scales exhibit the largest growth through a synergy between the Orr and the lift-up mechanisms and produce large streamwise streaks in the shear flow without an effect on the free surface. For large Froude numbers or large values of the shear, planar perturbations with larger horizontal scales exhibit the largest energy growth by effectively instigating the modal instability and excite surface waves at large amplitude.

DOI: [10.1103/PhysRevFluids.2.023901](https://doi.org/10.1103/PhysRevFluids.2.023901)

I. INTRODUCTION

Shear flows with an upper free surface arise naturally both in geophysical flows and in engineering applications. At the surface of the ocean, large-scale nonuniform currents [1] or smaller-scale currents such as the ones found at the crest of a spilling breaker [2,3], or in viscous ship wakes [4] are ubiquitous and typically break into turbulent mixing layers [5]. In engineering applications such as a proposed design for liquid walls and blankets in fusion reactors, liquid jets emanating from a nozzle develop a shear layer beneath the free surface and surface gravity waves emerge and break producing turbulence [6].

Previous studies showed that a mean subsurface shear overlying a stationary layer of infinite depth is unstable to two-dimensional planar perturbations with streamwise (zonal) wave numbers within a limited range [5,7]. Triantafyllou and Dimas [4] found two kinds of normal mode instabilities in the shear flow observed in experiments of wakes behind a hydrofoil: branch I modes at low wave numbers that resemble the varicose modes in an infinite flow and branch II modes at higher wave numbers that resemble the unstable modes found by Stern and Adam [5]. Bakas and Ioannou [8] (BI) used a piecewise linear velocity profile that possesses the same instability branches [9] and gained further insight into the instability mechanism by showing that the instability arises as the interaction between vorticity and gravity edge waves at the interfaces of vorticity and density discontinuities.

As shown by many theoretical studies [10–12] starting with the pioneering work of Taylor [13], Goldstein [14], and Bretherton [15], edge waves at the interfaces of density and/or vorticity discontinuities interact by inducing velocities at the other waves' interfaces that modify the other waves' amplitudes and phase speeds. Normal mode instability occurs when the waves resonate, that is, when their phases lock and propagate with the same phase speed in a growing configuration. This analysis can also be generalized in flows with magnetic fields [16,17]. Bakas and Ioannou showed that

*nbakas@uoi.gr

in the limit of small Froude number in which the free-surface displacement is infinitesimally small, the dominant interaction is the one between the two counterpropagating vorticity edge waves and the unstable mode resulting from this interaction corresponds to branch I instability of Triantafyllou and Dimas [4]. In the limit in which the mean flow vorticity extends until the surface, only the lower vorticity and the surface waves interact as the upper interface of vorticity discontinuity along with the upper vorticity wave vanishes. The resulting unstable mode corresponds to branch II instability of Triantafyllou and Dimas [4].

Even though the modal stability determines perturbation growth at large times, shear flows typically exhibit growth that is substantially faster than that predicted by the normal modes over intermediate-time scales [18,19]. Using generalized stability theory [18], BI assessed nonmodal perturbation growth of two-dimensional perturbations at finite time and showed that for wave numbers within the two instability branches, composite nonmodal perturbations can energize the instability at enhanced amplitude, while perturbations with wave numbers outside the instability branches exhibit explosive growth that is comparable to the growth obtained by perturbing the flow with the most unstable mode.

In this work we extend the analysis of BI and investigate the stability of a shear flow with a free surface with respect to three-dimensional perturbations in the Boussinesq limit. While three-dimensional (3D) modal instabilities in shear flows are typically slower than their 2D counterparts [20], 3D perturbations attain nonmodal growth that can be much larger than the growth attained by 2D perturbations confined to the shear plane [21–23]. The nonmodal growth of three-dimensional perturbations is the result of two mechanisms. The first is the 2D Orr mechanism in which perturbations tilted against the shear grow transiently as they shear over. The second mechanism is the lift-up effect [19,24,25], in which the cross-stream perturbation velocity tilts up the background spanwise vorticity producing large amplification of the streamwise velocity. In this study we first adopt the piecewise continuous velocity profile of Longuet-Higgins [9], which allows analytical work and the investigation of the modal stability and its characteristics by considering the interaction of 3D edge waves. Modal stability with respect to 3D perturbations was considered by Drivas and Wunsch [26], but for the shear layer lacking the upper layer of constant velocity and focusing on low Froude numbers for which the flow is modally stable. In this work we examine modal instability for a wide range of Froude numbers. We then address nonmodal perturbation growth by calculating the initial perturbations leading to the largest energy growth at finite time as well as calculating the corresponding growth achieved. We examine in detail both kinetic energy growth confined in the shear layer below the surface and excitation of surface waves with large amplitude.

This paper is organized as follows. In Sec. II we describe the linear evolution equations for three-dimensional perturbations in a horizontal shear flow with a free surface and investigate in Sec. III the emerging instabilities in terms of the interactions between the 3D vorticity and gravity edge waves propagating at the interfaces of vorticity and density discontinuities. In Sec. IV we calculate nonmodal growth of perturbations for a wide range of Froude numbers and examine the mechanisms leading to transient growth in detail. We finally end with a brief discussion and our conclusions in Sec. V.

II. FORMULATION OF THE STABILITY PROBLEM

Consider a homogeneous incompressible and inviscid fluid with density $\rho_m = \rho_0 \Theta(-z)$ in the unbounded region $z < 0$, where z is the vertical coordinate and Θ is the Theta function. At equilibrium, the fluid is hydrostatically balanced by pressure $p_0(z)$, the free surface of the fluid is flat at $z = 0$, and the velocity $U(z)$ in the streamwise (zonal) direction x is given by

$$U(z) = \begin{cases} V_0 & \text{for } -H_1 < z \leq 0 \\ V_0(z + H_2)/(H_2 - H_1) & \text{for } -H_2 < z \leq -H_1 \\ 0 & \text{for } z \leq -H_2 \end{cases} \quad (1)$$

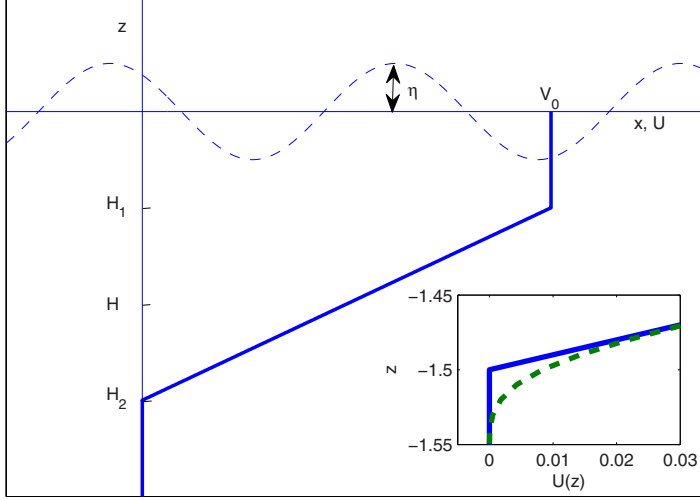


FIG. 1. Velocity profile $U(z)$ (solid line). The dashed line shows qualitatively the displacement η of the free surface from the equilibrium position $z = 0$. The inset shows the difference between the piecewise linear profile (solid line) used to analytically address the modal stability of the flow and the profile with rounded corners (dashed line) used to address the nonmodal stability.

and is shown in Fig. 1. Consider now small perturbations in the streamwise (zonal) x , spanwise (meridional) y , and vertical z directions u , v , and w , respectively, superimposed on the mean zonal flow $U(z)$, and perturbations in pressure p and density ρ superimposed on the mean pressure $p_0(z)$ and density ρ_0 , respectively. The perturbations evolve according to the nondimensional equations

$$[\partial_{\tilde{t}} + \tilde{U}(\tilde{z})\partial_{\tilde{x}}]\tilde{u} + \frac{d\tilde{U}}{d\tilde{z}}\tilde{w} = -\partial_{\tilde{x}}\tilde{p}, \quad (2)$$

$$[\partial_{\tilde{t}} + \tilde{U}(\tilde{z})\partial_{\tilde{x}}]\tilde{v} = -\partial_{\tilde{y}}\tilde{p}, \quad (3)$$

$$[\partial_{\tilde{t}} + \tilde{U}(\tilde{z})\partial_{\tilde{x}}]\tilde{w} = -\partial_{\tilde{z}}\tilde{p} - \frac{\tilde{\rho}}{F^2}, \quad (4)$$

$$[\partial_{\tilde{t}} + \tilde{U}(\tilde{z})\partial_{\tilde{x}}]\tilde{\rho} + \tilde{w}\delta(\tilde{z}) = 0. \quad (5)$$

In Eqs. (2)–(5), length scales are nondimensionalized by the mean depth of the shear layer $H = (H_1 + H_2)/2$, velocities are nondimensionalized by the maximum velocity V_0 , time is nondimensionalized by the shear time scale H/V_0 , and density and pressure are nondimensionalized by ρ_0 and $\rho_0 V_0^2$, respectively. Here $F = V_0/\sqrt{gH}$ is the Froude number based on the mean velocity of the fluid V_0 at the surface and the mean depth of the shear layer H . The nondimensional quantities are denoted by the tildes and we hereafter drop the tildes for simplicity of notation. The nondimensional mean velocity is

$$U(z) = \begin{cases} 1 & \text{for } -h_1 < z \leq 0 \\ \alpha(z + h_2) & \text{for } -h_2 < z \leq -h_1 \\ 0 & \text{for } z \leq -h_2, \end{cases} \quad (6)$$

where $h_1 = H_1/H$, $h_2 = H_2/H$, and $\alpha = 1/(h_2 - h_1)$ is the nondimensional shear. Note that because $h_1 + h_2 = 2$, the only nondimensional free parameters are the Froude number and the nondimensional shear $\alpha = 1/2(1 - h_1)$. The delta function in Eq. (5) arises as the mean density is discontinuous at the surface. In addition, the velocities satisfy the continuity equation

$$\partial_x u + \partial_y v + \partial_z w = 0 \quad (7)$$

and the small free-surface elevation $\eta(x, y, t)$ satisfies the linearized kinematic condition

$$(\partial_t + \partial_x)\eta = w|_{z=0}. \quad (8)$$

Comparison of (8) to (5) yields

$$\rho = \eta\delta(z). \quad (9)$$

Consider plane-wave solutions of the form

$$[u, v, w, \rho, \eta, p]^T = [\hat{u}(z, t), \hat{v}(z, t), \hat{w}(z, t), \hat{\rho}(z, t), \hat{\eta}(t), \hat{p}(z, t)]^T e^{ikx + ily}. \quad (10)$$

By first calculating the divergence of (2)–(4), we obtain the diagnostic equation for pressure

$$(\partial_{zz}^2 - K^2)\hat{p} = -2\frac{dU}{dz}ik\hat{w} - \frac{1}{F^2}\partial_z\hat{\rho}, \quad (11)$$

where $K = \sqrt{k^2 + l^2}$ is the horizontal wave number. Taking the Laplacian of (4) and using (9) and (11), we obtain

$$[\partial_t + ikU(z)](\partial_{zz}^2 - K^2)\hat{w} - \frac{d^2U}{dz^2}ik\hat{w} = \frac{K^2}{F^2}\hat{\eta}\delta(z). \quad (12)$$

We then eliminate pressure from (2) and (3) to obtain the equation for the evolution of the vertical component of vorticity $\hat{\zeta} = ik\hat{v} - il\hat{u}$:

$$[\partial_t + ikU(z)]\hat{\zeta} + \frac{dU}{dz}il\hat{w} = 0. \quad (13)$$

Finally, the free surface evolves as

$$(\partial_t + ik)\hat{\eta} = \hat{w}|_{z=0}. \quad (14)$$

Equations (12)–(14) form a closed system that governs the evolution of vorticity, vertical velocity, and free-surface displacement of the plane waves.

III. MODAL STABILITY

In this section we follow BI and study the modal stability of the flow in terms of the interaction between edge waves. The edge waves are supported at the three surfaces of discontinuity in the flow. At the free surface where the mean density ρ_m is discontinuous $d\rho_m/dz = -\delta(z)$ and at depths h_1 and h_2 where the mean vorticity dU/dz is discontinuous $d^2U/dz^2 = \alpha[-\delta(z + h_1) + \delta(z + h_2)]$. To obtain the dispersion relation for the edge waves, we first note that away from these interfaces the vertical velocity evolves according to

$$[\partial_t + ikU(z)](\partial_{zz}^2 - K^2)\hat{w} = 0. \quad (15)$$

The surface edge waves satisfy (15) away from $z = 0$ and (13) as well as the kinematic boundary condition (14) at the free surface and the boundedness condition at $z \rightarrow -\infty$,

$$|\hat{w}(z \rightarrow -\infty)| < \infty. \quad (16)$$

Integrating (15) and applying the boundary conditions (14) and (16) yields

$$\hat{w} = -\frac{1}{K}e^{Kz}e^{-ikt \pm i\sqrt{K}t/F}. \quad (17)$$

The waves manifest close to the surface as they decay exponentially with depth and satisfy the dispersion of three-dimensional surface gravity waves.

The vorticity edge waves supported at $z = -h_j$ with $j = 1, 2$ satisfy (15) away from $z = -h_j$ and also (13). By integrating (12) close to the interface of vorticity discontinuity $z = -h_j$, we obtain

the additional condition

$$\partial_z \hat{w}|_{z=-h_j^+} - \partial_z \hat{w}|_{z=-h_j^-} = (-1)^{j+1} i k \alpha \hat{w}|_{z=-h_j}, \quad (18)$$

which is satisfied at $z = -h_j$. Following previous studies [11,12], we isolate the vorticity edge waves from the surface edge waves by assuming that the vorticity waves have a zero imprint at the surface $\hat{\eta} = 0$. Under this assumption and integrating (12) close to the surface, we obtain the surface boundary condition

$$\partial_z w|_{z=0} = 0. \quad (19)$$

In addition, the edge-wave solution is required to be bounded at $z \rightarrow -\infty$ [see Eq. (16)]. Integrating (15) and applying the boundary conditions (16), (18), and (19), we obtain

$$\hat{w} = -\frac{1}{2K} (e^{-K|z+h_j|} + e^{K(z-h_j)}) e^{-ikc_j t}, \quad (20)$$

where

$$c_j = U_j + (-1)^j \frac{\alpha}{2K} (1 + e^{-2Kh_j}), \quad (21)$$

with $U_j = U|_{z=-h_j}$. The edge wave supported at the upper interface of discontinuity ($j = 1$) propagates retrograde relative to the mean flow U_1 , while the wave supported at the lower interface of discontinuity ($j = 2$) propagates prograde relative to the mean flow U_2 , forming a pair of counterpropagating Rossby waves [27].

The normal modes are synthesized by superposing the edge waves

$$\hat{w}(z, t) = -\frac{q_0(t)}{K} e^{Kz} - \frac{q_1(t)}{2K} (e^{-K|z+h_1|} + e^{K(z-h_1)}) - \frac{q_2(t)}{2K} (e^{-K|z+h_2|} + e^{K(z-h_2)}), \quad (22)$$

which can interact with each other through the vertical velocity that each wave imposes on the interfaces of the others. Each wave can then affect the amplitude and the phase of the other waves with the modal solutions corresponding to the phase-locked configuration. If the phase difference in the phase-locked configuration is such that the waves reenforce each other, then the normal mode is exponentially growing.

Substituting (22) into (12), integrating close to $z = 0$, $z = -h_1$, and $z = -h_2$, and using the kinematic condition (14), we obtain that the amplitudes of the edge waves evolve according to

$$\frac{d\mathbf{x}_e}{dt} = \mathbf{A}_e \mathbf{x}_e, \quad (23)$$

where $\mathbf{x}_e = [q_0(t), \eta(t), q_1(t), q_2(t)]^T$ is the state vector and

$$\mathbf{A}_e = \begin{pmatrix} -ik & K^2/F^2 & 0 & 0 \\ -1/K & -ik & -e^{-Kh_1}/K & -e^{-Kh_2}/K \\ i\sigma_{10} & 0 & -ikc_1 & i\sigma_{12} \\ -i\sigma_{20} & 0 & -i\sigma_{12} & -ikc_2 \end{pmatrix}, \quad (24)$$

with c_1 and c_2 the phase speeds of the vorticity edge waves given by (21) and $\sigma_{10} = k\alpha e^{-Kh_1}/K$, $\sigma_{20} = k\alpha e^{-Kh_2}/K$, and $\sigma_{12} = k\alpha(e^{-K(h_2-h_1)} + e^{-2K})/2K$ coefficients that measure the strength of the interaction between the edge waves, as we will see shortly. Matrix \mathbf{A}_e describes the interaction between the surface waves and the vorticity waves and its eigenvalues λ and eigenvectors determine the frequencies, growth rates, and vertical structure of the normal modes. Figure 2(a) shows the maximum growth rate $\sigma = \max[\text{Re}(\lambda)]$ obtained through eigenanalysis of \mathbf{A}_e , as a function of the total wave number K and the angle $\theta = \arctan(l/k)$ that the phase lines form with respect to the y direction for $F = 1$ and $\alpha = 1$. As in the case of 2D perturbations ($\theta = 0$), there are two branches of instability: branch I instability of Triantafyllou and Dimas [4] at low wave numbers and branch II

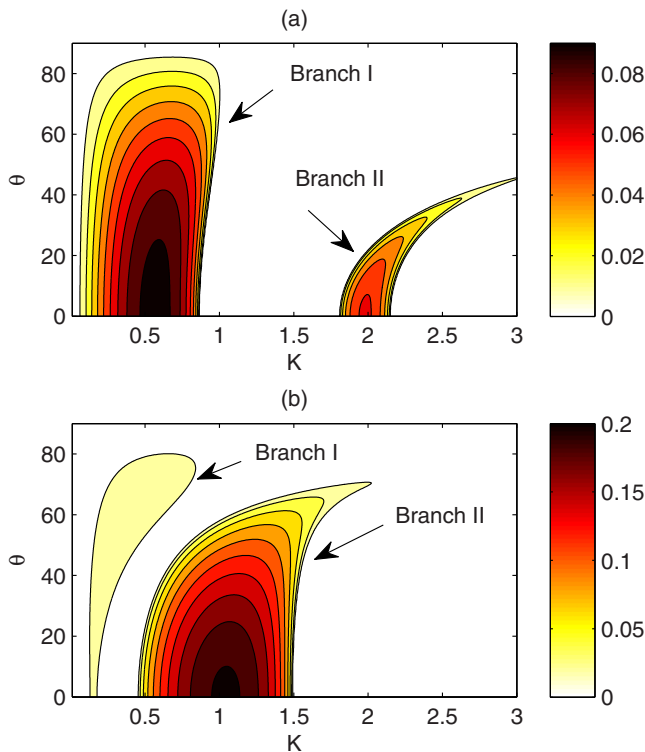


FIG. 2. Growth rate σ of the unstable normal modes as a function of the horizontal wave number $K = \sqrt{k^2 + l^2}$ and the angle $\theta = \arctan(l/k)$ for (a) $F = 1$ and (b) $F = 3$. In both panels the shear is $\alpha = 1$.

at intermediate wave numbers that are designated in Fig. 2. For both branches, the maximum growth rate occurs for planar perturbations in the x - z plane ($\theta = 0$), consistent with Squire's theorem [20], which also holds for fluids with a free surface [28]. Note, however, that for plane-wave perturbations with $K > 2.15$, planar perturbations are neutral, while oblique 3D perturbations with $2.15 < K < 3$ are exponentially growing. As a result, modal stability analysis with respect to 2D perturbations accurately predicts the fastest growing exponential perturbations in the flow, but underestimates the range of scales for the unstable perturbations. For larger Froude numbers shown in Fig. 2(b), branch II instability that has now shifted to larger-scale perturbations dominates modal perturbation growth. Similar to the case of $F = 1$, the range of scales for the 3D unstable perturbations is larger compared to the corresponding range of planar 2D perturbations, however planar perturbations exhibit the fastest growth. The maximum growth rate over all wave numbers $\sigma_{\max} = \max_{K, \theta} \sigma$ is shown as a function of Froude number in Fig. 3. As also noted by Longuet-Higgins [9], for small Froude numbers, low wave numbers of branch I instability dominate the growth, while for large Froude numbers smaller scales of branch II instability dominate, with the two branches having comparable growth rates for Froude numbers of $O(1)$. Note also that the growth rate asymptotes to a constant value for large Froude numbers. The sensitivity of these results on the shear is shown in Fig. 4. We observe that the domain of unstable wave numbers in both branches increases with the shear with the branches merging for large values of the shear [see Fig. 4(d)]. Furthermore, the growth rates increase monotonically with the shear.

In order to gain insight into the modal instability arising from the interaction of the edge waves and provide an explanation for the decrease of the growth rate with the angle θ and the larger range of scales for the unstable perturbations, we follow the analysis in Ref. [27] and study the evolution

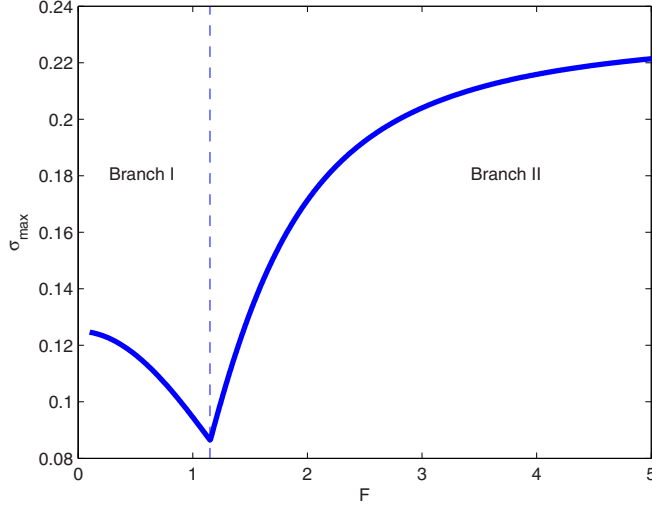


FIG. 3. Maximum value of the growth rate σ_{\max} over all perturbations as a function of the Froude number. The regions in F where branch I and branch II instabilities dominate is also indicated. The shear is $\alpha = 1$.

of the amplitude and phase of each edge wave separately by writing the complex amplitudes as

$$[q_0(t), \eta(t), q_1(t), q_2(t)]^T = [Q_0(t)e^{i\epsilon_0(t)}, H(t)e^{i\epsilon_\eta(t)}, Q_1(t)e^{i\epsilon_1(t)}, Q_2(t)e^{i\epsilon_2(t)}]^T. \quad (25)$$

Plugging (25) into (23) and taking the real and imaginary parts separately, we obtain the equations for the evolution of the amplitude of the edge waves

$$\frac{dQ_0}{dt} = \frac{K^2}{F^2} H \cos \epsilon_{\eta 0}, \quad (26a)$$

$$\frac{dH}{dt} = -\frac{Q_0}{K} \cos \epsilon_{\eta 0} - \frac{e^{-Kh_1}}{K} Q_1 \cos(\epsilon_{10} - \epsilon_{\eta 0}) - \frac{e^{-Kh_2}}{K} Q_2 \cos(\epsilon_{20} - \epsilon_{\eta 0}), \quad (26b)$$

$$\frac{dQ_1}{dt} = \sigma_{10} Q_0 \sin \epsilon_{10} + \sigma_{12} Q_2 \sin \epsilon_{12}, \quad (26c)$$

$$\frac{dQ_2}{dt} = -\sigma_{20} Q_0 \sin \epsilon_{20} + \sigma_{12} Q_1 \sin \epsilon_{12}, \quad (26d)$$

where $\epsilon_{\eta 0} = \epsilon_\eta - \epsilon_0$ and $\epsilon_{ij} = \epsilon_i - \epsilon_j$, with $i, j = 0, 1, 2$, are the phase differences between the edge waves. The amplitude tendencies depend on the strength of the interaction σ_{10} , σ_{20} , and σ_{12} and on the phase differences between the waves. The phase differences evolve according to

$$\frac{d\epsilon_{\eta 0}}{dt} = \frac{F^2 Q_0^2 - K^3 H^2}{F^2 K Q_0 H} \sin \epsilon_{\eta 0} - \frac{\sigma_{10} Q_1}{\alpha k H} \sin(\epsilon_{10} - \epsilon_{\eta 0}) - \frac{\sigma_{20} Q_2}{\alpha k H} \sin(\epsilon_{20} - \epsilon_{\eta 0}), \quad (27a)$$

$$\frac{d\epsilon_{10}}{dt} = k(1 - c_1) + \sigma_{10} \frac{Q_0}{Q_1} \cos \epsilon_{10} + \sigma_{12} \frac{Q_2}{Q_1} \cos \epsilon_{12} - \frac{K^2 H}{F^2 Q_0} \sin \epsilon_{\eta 0}, \quad (27b)$$

$$\frac{d\epsilon_{20}}{dt} = k(1 - c_2) - \sigma_{20} \frac{Q_0}{Q_2} \cos \epsilon_{20} - \sigma_{12} \frac{Q_1}{Q_2} \cos \epsilon_{12} - \frac{K^2 H}{F^2 Q_0} \sin \epsilon_{\eta 0}, \quad (27c)$$

$$\frac{d\epsilon_{12}}{dt} = -k(c_1 - c_2) + \sigma_{10} \frac{Q_0}{Q_1} \cos \epsilon_{10} + \sigma_{20} \frac{Q_0}{Q_2} \cos \epsilon_{20} + \sigma_{12} \frac{Q_1^2 + Q_2^2}{Q_1 Q_2} \cos \epsilon_{12}. \quad (27d)$$

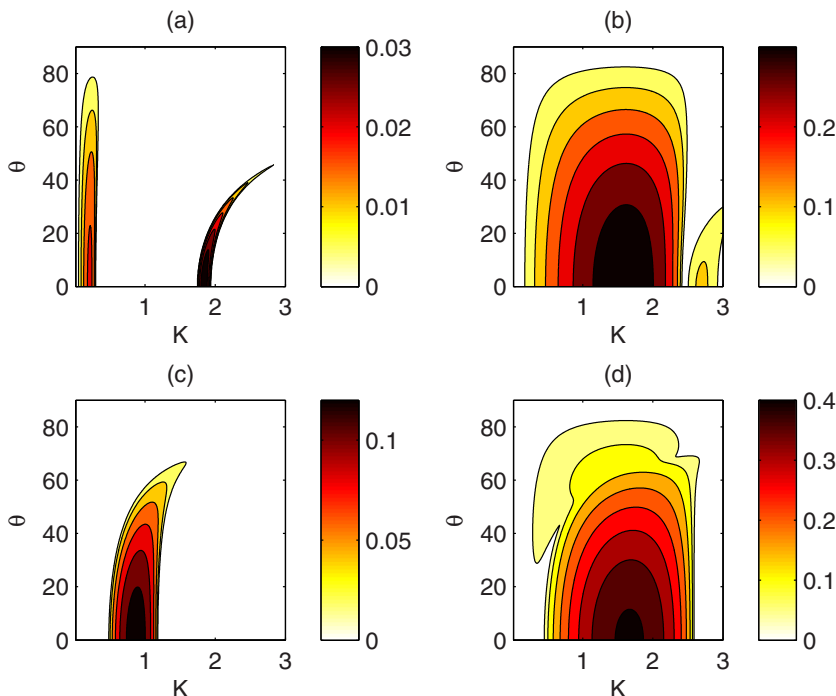


FIG. 4. Growth rate σ of the unstable normal modes as a function of the horizontal wave number $K = \sqrt{k^2 + l^2}$ and the angle $\theta = \arctan(l/k)$ for $F = 1$ and (a) $\alpha = 2/3$ and (b) $\alpha = 2$. (c) and (d) Same as in (a) and (b) but for Froude number $F = 3$.

The phase of each wave changes linearly according to its phase speed [the first terms on the right-hand sides of (27b)–(27d)] and due to the effect of the other waves. The phases lock when the influence of the other waves is large enough to match the differing phase speeds of the waves. The normal modes correspond to the phase-locked configuration in which the left-hand side of (27) is equal to zero. If the phase differences in this configuration are, for example, $0^\circ < \epsilon_{10}$ and $\epsilon_{12} < 180^\circ$, then there is mutual growth of the edge-wave amplitudes and the normal mode is unstable with maximum possible amplitude growth achieved for $\epsilon_{10} = \epsilon_{12} = 90^\circ$ and $\epsilon_{20} = -90^\circ$.

The phase-locked configuration for 3D perturbations is similar to the corresponding configuration for planar perturbations discussed by BI and can be exemplified by focusing on the lower vorticity edge wave. The amplitude of the lower vorticity edge wave Q_2 is influenced by the action of the surface and the upper vorticity waves and its tendency depends on two factors [see Eq. (26d)]. The first factor is the strength of the two interactions σ_{20} and σ_{12} , which are both positive. The second factor is the phase-locked configuration in which the amplitudes Q_0 and Q_1 and the phase differences ϵ_{20} and ϵ_{12} assume specific values. Figure 5 illustrates the influence of the phase-locked configuration by plotting the two terms $Q_1 \sin \epsilon_{12}$ and $-Q_0 \sin \epsilon_{20}$ as a function of K and θ . Amplification of branch I unstable modes occurs, as the phase difference between the two vorticity edge waves in the phase-locked state is such that the upper vorticity wave induces a positive tendency $Q_1 \sin \epsilon_{12}$ at the interface of the lower vorticity wave [see Fig. 5(a)]. The phase-locked configuration for the most unstable mode with $K = 0.57$ and $\theta = 0$ is illustrated in Fig. 6(a). The phase difference $\epsilon_{12} \simeq 97^\circ$ between the upper and lower vorticity edge waves is such that the maximum tendency induced by the upper wave almost coincides with the maximum velocity of the lower wave (and the same at the upper wave's interface, which is not shown) leading to maximum mutual growth of the two vorticity edge waves. The surface waves have a stabilizing effect as the induced positive tendency coincides with negative velocity ($\epsilon_{20} \simeq 125^\circ$) leading to a negative tendency $-Q_0 \sin \epsilon_{20}$

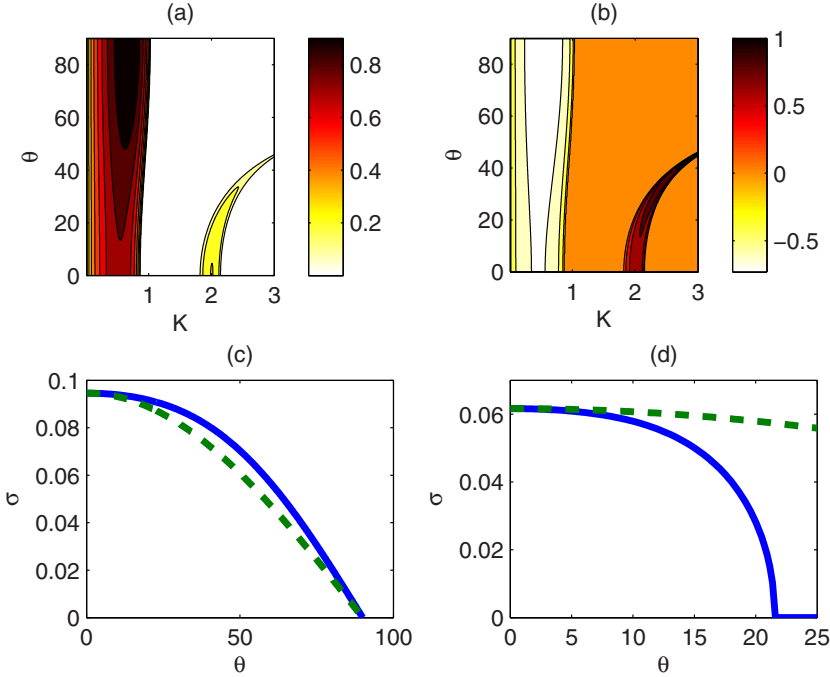


FIG. 5. (a) Amplitude tendency factor $Q_1 \sin \epsilon_{12} / Q_2$ induced by the upper vorticity edge wave at the lower wave's interface as a function of the horizontal wave number $K = \sqrt{k^2 + l^2}$ and the angle $\theta = \arctan(l/k)$. (b) Amplitude tendency factor $-Q_0 \sin \epsilon_{10} / Q_2$ induced by the surface edge wave at the lower vorticity wave's interface as a function of wave number K and wave-number angle θ . (c) and (d) Growth rate of the unstable wave of (c) branch I with $K = 0.57$ and (d) branch II with $K = 1.99$ as a function of the wave-number angle θ (solid line). The curve $\cos \theta$ normalized to have the same maximum amplitude is also shown for comparison (dashed line). In all panels the Froude number is $F = 1$ and $\alpha = 1$.

[see Fig. 5(b)] that counteracts part of the positive tendency induced by the upper vorticity wave. As a result, the growth rate of branch I instability decreases for larger Froude numbers and the instability region in wave-number space shrinks with only very small numbers being unstable, as shown in Fig. 2(b). Amplification for branch II unstable modes occurs as both the surface waves and the upper vorticity wave phase lock in a favorable configuration [see Fig. 6(b)] and produce positive tendencies [see Figs. 5(a) and 5(b)].

The higher growth rates of planar perturbations ($\theta = 0^\circ$) can be explained by focusing on the dependence of the phase-locked configuration and the dependence of the interaction strength on the angle θ . Figure 6(a) shows the edge-wave interaction for the unstable mode with $K = 0.57$ and $\theta = 45^\circ$ of branch I. The surface waves phase lock in an angle that enhances their stabilizing effect, leading to a more negative tendency factor $-Q_0 \sin \epsilon_{20}$ [see Fig. 5(b)]. The upper vorticity wave phase locks in an angle that demotes mutual growth compared to the phased-locked configuration of $\theta = 0^\circ$, but due to the higher amplitude Q_1 at the phased-lock state, the tendency factor $Q_1 \sin(\epsilon_{12})$ is enhanced and because it is typically larger than $-Q_0 \sin \epsilon_{20}$ we would expect higher growth rates with increasing angle. On the other hand, the interaction strengths of the edge waves σ_{20} and σ_{12} are proportional to the streamwise wave number $k = K \cos \theta$ and monotonically decay with θ . Figure 5(c) shows the growth rate for the most unstable wave number $K = 0.57$ of branch I as a function of angle θ along with $\cos \theta$. We observe that the monotonic decay of the growth rate is dominated by the reduction of the interaction strength as it follows closely the cosine curve, while the phase-locked configuration slightly offsets the decrease. For unstable modes in branch II, the

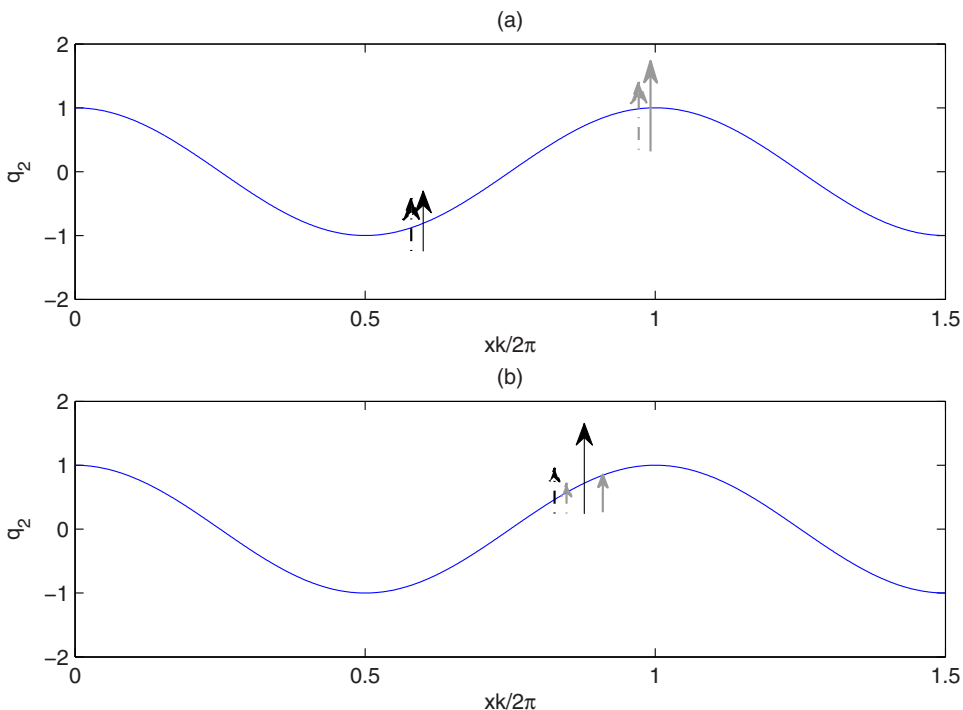


FIG. 6. Schematic illustration of the edge-wave interaction underlying (a) branch I and (b) branch II instability. (a) Vertical velocity anomaly of the lower vorticity edge wave (at $z = -h_2$). The black (gray) solid arrows show the vertical velocity tendency induced by the surface (vorticity) edge waves at $z = -h_2$ when the waves have phased locked in the configuration of the fastest growing normal mode of branch I instability ($K = 0.57$ and $\theta = 0^\circ$). The dash-dotted arrows show the induced tendencies in the phase-locked configuration of the normal mode with $K = 0.57$ and $\theta = 45^\circ$. (b) Same as in (a) but for the fastest growing normal mode in branch II with $K = 1.99$ and $\theta = 0^\circ$ (solid arrows) and for the normal mode with $K = 1.99$ and $\theta = 20^\circ$ (dash-dotted arrows).

upper and surface edge waves phase lock in a configuration that reduces their destabilizing effect [see Fig. 6(b)] and the destabilizing tendency factors decrease with θ [see Figs. 5(a) and 5(b)]. Since the growth rate decreases with a much faster pace than $\cos \theta$ [see Fig. 5(d)], the reduction with the angle is attributed mainly to the phase-locked configuration that is less favorable to mutual growth.

We investigate now the interaction dynamics underlying the increase of the domain of unstable wave numbers for 3D perturbations and the increase of the growth rate with the shear. Consider the case of branch II modes when the Froude number $F = 1$. The growth rate of planar 2D normal modes decreases with the wave number when $K > 2$ as phase locking occurs at angles that are less favorable to mutual growth of the edge waves. This is illustrated in Fig. 7. Figure 7(a) shows the four terms that determine the tendency of the phase difference between the vorticity waves as a function of wave number K [see Eq. (27d)]. Phase locking occurs as the differing phase speeds that linearly increase the phase difference [first term in Eq. (27d)] are mainly balanced by the change due to the interaction of the upper vorticity and the surface waves [second term in Eq. (27d)] and secondarily due to the interaction of the lower vorticity and the surface waves [third term in Eq. (27d)], while the interaction of the upper and the lower vorticity waves [last term in Eq. (27d)] has little influence. However, we observe that the main balancing second term decreases with wave number. The reason is that while the phase difference ϵ_{10} at the phase-locked configuration that is shown in Fig. 7(b) does not change significantly ($\cos \epsilon_{10} \simeq 1$ for this range of wave numbers), the interaction coefficient decreases exponentially with wave number. The differing phase speeds that are larger for smaller

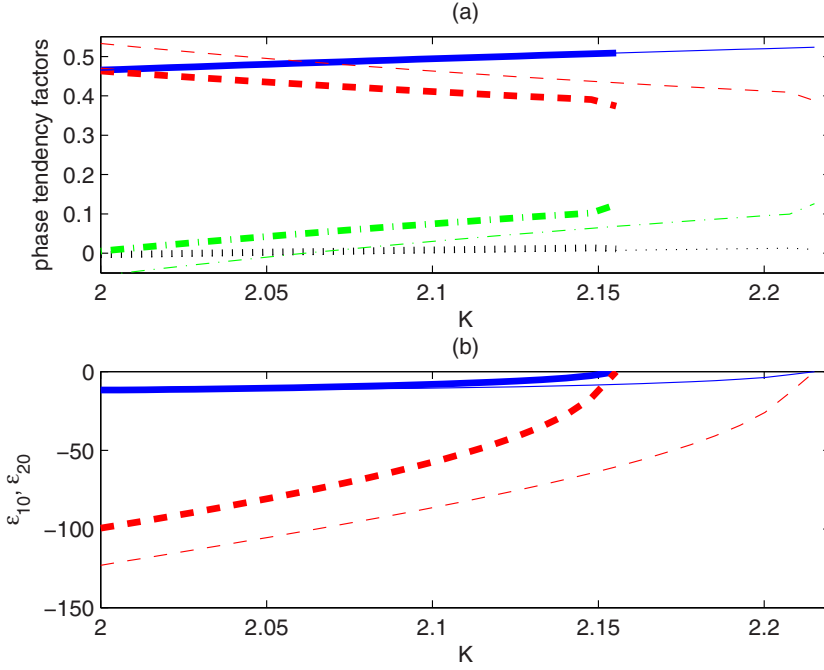


FIG. 7. (a) Tendency factors for the phase difference between the vorticity edge waves ϵ_{12} . Shown are the phase speed differences $c_1 - c_2$ (solid lines), $\sigma_{10} Q_0 \cos(\epsilon_{10}) / k Q_1$ (dashed lines), $\sigma_{20} Q_0 \cos(\epsilon_{20}) / k Q_2$ (dash-dotted lines), and $\sigma_{12} (Q_1^2 + Q_2^2) \cos(\epsilon_{12}) / k Q_1 Q_2$ (dotted lines) as a function of K for the phase-locked configuration of the normal modes with $\theta = 0^\circ$ (thick lines) and $\theta = 15^\circ$ (thin lines). (b) Phase differences ϵ_{10} (solid lines) and ϵ_{20} (dashed lines) at the phase-locked configuration as a function of wave number K for the normal modes with $\theta = 0^\circ$ (thick lines) and the modes with $\theta = 15^\circ$ (thin lines).

scales have to be balanced then by the third term. This is achieved by the rapid decrease of the phase difference ϵ_{20} [see Fig. 7(b)], which, however, is at the expense of mutual growth that depends on $\sin \epsilon_{20}$. For $K > 2.15$, all angles have decreased to zero and phase locking occurs only at a stable configuration. Oblique edge waves that are also shown in Fig. 7 are able to phase lock in a growing configuration for larger wave numbers, as the phase difference ϵ_{20} is larger for lower wave numbers. As discussed above, this leads, on the one hand, to a less favorable configuration of the most unstable modes with $K \simeq 2$ but, on the other hand, it allows for $\epsilon_{20} \neq 0$ for a wider range of wave numbers. Finally, the monotonic increase of the growth rates with the shear can be attributed to the linear increase of the intensity of the edge wave interaction with α .

IV. NONMODAL GROWTH

In realistic geophysical and laboratory flows, perturbation growth occurs over a finite-time interval. It is therefore of interest to find the initial conditions yielding the largest perturbation growth typically measured by the energy norm over a specified time interval T_{opt} . Such a generalized stability analysis is important for two reasons. The first is that nonorthogonality of the modes of the linear operator governing perturbation dynamics allows for transient growth even in regions of the parameter space in which the flow is modally stable. The second is that composite initial perturbations distinct from the unstable normal modes can lead to larger perturbation growth compared to what is obtained by the normal modes. As a result, modal stability analysis can be deficient in predicting both the scales and the growth rate of perturbations in a shear flow as well as transition to turbulence [18,19,29].

Transient growth results from the contribution of both the discrete part of the spectrum involving the interaction of the edge waves and the singular continuous spectrum of the linear operator governing perturbation dynamics, but as was shown by BI for planar perturbations, the contribution of the singular spectrum in nonmodal growth is dominant. There are two physical mechanisms for transient growth of three-dimensional perturbations due to the singular continuous spectrum in shear flows, which are exemplified by considering a constant shear flow that lacks a discrete spectrum. The first is the Orr mechanism [30] in which 2D plane waves conserve spanwise vorticity $q = \partial_z u - \partial_x w$. As the waves are sheared over and their vorticity is spatially deformed, the velocities must change accordingly to conserve vorticity. This leads to energy amplification of waves with phase lines leaning against the shear with vertical velocity peaking at the moment at which the phase lines are perpendicular to the planar flow. As the perturbations subsequently lean with the shear, their energy decays. The second is the lift-up effect that produces linear growth of streamwise independent perturbations [22,24,25]. In this case vertical vorticity is generated through tilting of the background vorticity by the perturbation [see Eq. (13)], leading to the generation of large velocity streaks in the flow.

Recently, two alternative interpretations of the transient growth mechanisms were put forward by Chagelishvili *et al.* [31] and Vitoshkin *et al.* [32]. Chagelishvili *et al.* [31] showed that the energy exchange between the mean flow and the perturbations can be viewed mechanistically as resulting from the interplay of the elastic collision of fluid particles with the planes of constant pressure and the shear flow kinematics. Vitoshkin *et al.* [32] stressed the importance of vortex stretching. They found that the spanwise vorticity that is forced by the divergence on the plane of the flow $d = \partial_x u + \partial_z w$ and the divergence itself exhibit mutual growth when the two fields are out of phase (in the present choice of geometry) and the perturbations lean with the shear. For three-dimensional perturbations, the synergy between these two mechanisms can lead to explosive perturbation growth that exceeds growth of planar perturbations [22,23].

To investigate transient perturbation growth in this case, we consider the mean velocity profile used by Lindzen and Barker [33] that differs from the profile given in Eq. (1) only in that the corners at the edges of the shear within a region of width $2\delta z = 0.2$ have been smoothed out as shown in the inset of Fig. 1. Note that the modal stability properties do not depend sensitively on the modification of the profile with the growth rates obtained for the rounded corner profile differing only by less than 5% compared to the growth rates obtained for the piecewise linear profile reported in the previous section. We write (12)–(14) in the compact form

$$\frac{d\mathbf{x}}{dt} = \mathbf{A}\mathbf{x}, \quad (28)$$

where $\mathbf{x} = [\hat{\zeta}, \hat{w}, \hat{\eta}]^T$ is the state vector and

$$\mathbf{A} = \begin{pmatrix} -ikU & -il\frac{dU}{dz} & 0 \\ 0 & (\partial_{zz}^2 - K^2)^{-1}[-ikU(\partial_{zz}^2 - K^2) + ik\frac{d^2U}{dz^2}] & \frac{K^2}{F^2}\delta(z) \\ 0 & \delta(z) & -ik \end{pmatrix} \quad (29)$$

is the linear operator governing perturbation dynamics. We discretize the fields in \mathbf{x} in a grid with N collocation points spanning the range $-h_d \leq z \leq 0$ and take a zero boundary condition for the vertical velocity \hat{w} at the bottom of the domain $z = -h_d$. The fields \mathbf{x} become $N \times 1$ vectors and the differential operators in Eq. (29) become $N \times N$ matrices. The horizontally averaged perturbation energy

$$E = \frac{1}{2} \overline{\left(u^2 + v^2 + w^2 + \frac{1}{F^2} \eta^2 \right)} = \int_{-\infty}^0 \frac{1}{4} (|\hat{u}|^2 + |\hat{v}|^2 + |\hat{w}|^2) dz + \frac{1}{F^2} |\hat{\eta}|^2, \quad (30)$$

which changes through the Reynolds stress \overline{uw} ,

$$\frac{dE}{dt} = -\overline{uw} = - \int_{-\infty}^0 \frac{1}{2} \frac{dU}{dz} \text{Re}(\hat{u}\hat{w}^*) dz, \quad (31)$$

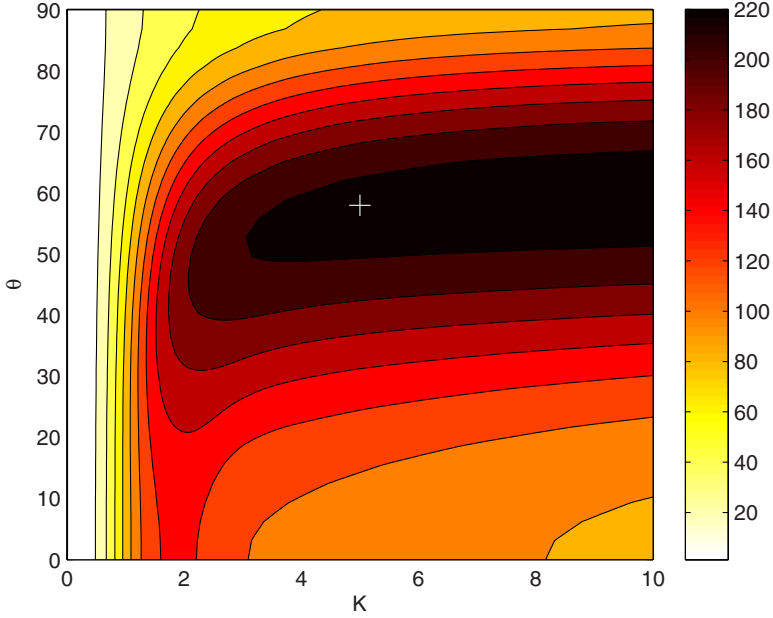


FIG. 8. Optimal energy growth $G(T_{\text{opt}})$ as a function of horizontal wave number K and wave-number angle θ . The wave number and angle of the optimally growing perturbation shown in Fig. 9 is indicated by the plus, the optimization time is $T_{\text{opt}} = 10$, the Froude number is $F = 1$, and $\alpha = 1$.

can be written in the bilinear form $E = \mathbf{x}^\dagger \mathbf{M} \mathbf{x}$, where \mathbf{M} is the energy metric and the dagger denotes the Hermitian transpose. For the reported calculations we used $N = 600$ grid points for which numerical convergence is achieved. The depth of the domain was taken to be far from the shear at $h_d = 8$ and the results proved to be insensitive to a further increase of h_d . As in the previous section, the shear is $\alpha = 1$ for most of the cases shown and the sensitivity of the results on the shear is discussed later on. The largest energy growth $G(T_{\text{opt}})$ that can be achieved over the specified time interval T_{opt} by any initial perturbation of unit energy

$$G(T_{\text{opt}}) = \max \frac{\mathbf{x}^\dagger(T_{\text{opt}}) \mathbf{M} \mathbf{x}(T_{\text{opt}})}{\mathbf{x}^\dagger(0) \mathbf{M} \mathbf{x}(0)} \quad (32)$$

can be calculated from the generalized eigenanalysis

$$\Phi(T_{\text{opt}}) \mathbf{v} = \mu \mathbf{M} \mathbf{v}, \quad (33)$$

where $\Phi(T_{\text{opt}}) = e^{A^\dagger T_{\text{opt}}} \mathbf{M} e^{A T_{\text{opt}}}$. The maximum eigenvalue μ is the optimal growth G , while the corresponding eigenvector \mathbf{v} is the optimal initial perturbation [18].

The optimizing time T_{opt} is typically chosen as the time scale of breaking initiation or the time scale over which turbulent fluctuations disrupt perturbation growth. Although the geometry taken in this study is simplified to allow for a comprehensive understanding and is not aiming at directly addressing realistic flows, experiments investigating ship wakes [4] or spilling breakers [34] suggest a time scale of the order of ten nondimensional advective time units. We choose this value in most of the calculations and discuss the sensitivity of the obtained results for other values of T_{opt} of the same order. The optimal energy growth G achieved for $T_{\text{opt}} = 10$ is shown in Fig. 8 as a function of the horizontal wave number K and the wave-number angle $\theta = \arctan(l/k)$. We can see that the maximum optimal growth of a 200-fold increase of initial energy is achieved by oblique 3D perturbations having $\theta_{\text{max}} \simeq 60^\circ$ and small scales (G reaches a plateau with K), even though the fastest exponentially growing perturbations are planar and have lower wave numbers [see Fig. 2(a)].

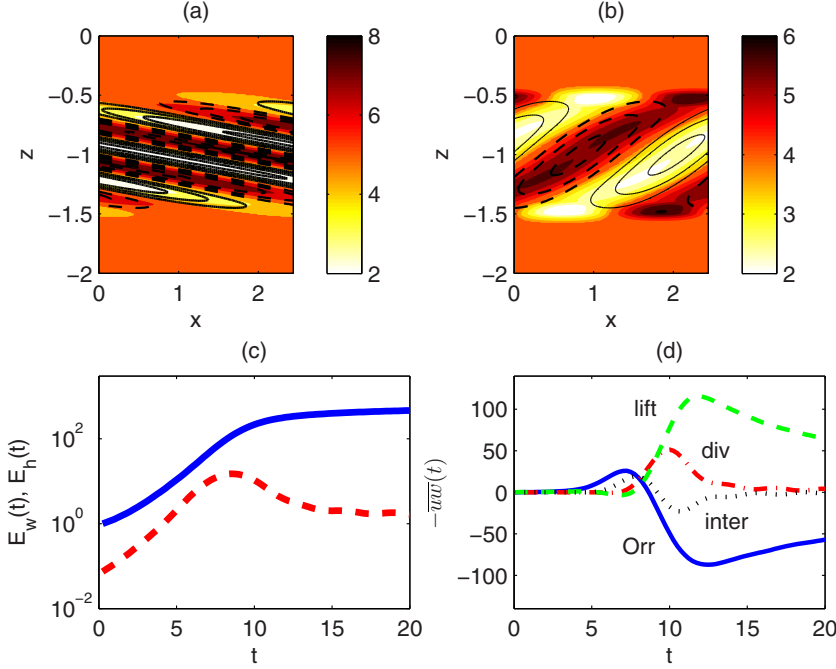


FIG. 9. (a) Structure of the optimally growing perturbation with wave number and phase angle marked by the plus in Fig. 8. Shown are contours of the spanwise component of vorticity $q = \partial_z u - \partial_x w$ (shades) and contours of divergence in the plane of the flow $d = \partial_x u + \partial_z w$ (lines). The contour interval is two and positive (negative) values of d are indicated with solid (dashed) lines. (b) Same as in (a) but for the structure of the evolved optimal perturbation at the optimization time $T_{\text{opt}} = 10$. (c) Contributions of the horizontal components of velocity $\overline{E}_h = (1/2)u^2 + v^2$ (solid line) and vertical component of velocity $\overline{E}_w = (1/2)w^2$ (dashed line) in the total energy evolution for the maximally growing perturbation. (d) Contributions of the four components in the Reynolds stress. Shown are the contributions of the rotational part $-\overline{uw}_{\text{Orr}}$ (solid line), the divergent part $-\overline{uw}_{\text{div}}$ (dash-dotted line), the first mixed rotational-divergent term $-\overline{uw}_{\text{lift}}$ (dashed line), and the second mixed rotational-divergent term $-\overline{uw}_{\text{inter}}$ (dotted line).

To investigate the mechanisms leading to energy growth we follow Bakas [35] and Vitoshkin *et al.* [32] and decompose the velocities in the plane of the flow into a rotational and a divergent part with the aid of a stream function ψ and a velocity potential ϕ ,

$$[u, w]^T = [u_q + u_d, w_q + w_d]^T = [-\partial_z \psi + \partial_x \phi, \partial_x \psi + \partial_z \phi]^T. \quad (34)$$

The Reynolds stress is then decomposed accordingly

$$\overline{uw} = \underbrace{\overline{u_q w_q}}_{\overline{uw}_{\text{Orr}}} + \underbrace{\overline{u_d w_d}}_{\overline{uw}_{\text{div}}} + \underbrace{\overline{u_q w_d}}_{\overline{uw}_{\text{lift}}} + \underbrace{\overline{u_d w_q}}_{\overline{uw}_{\text{inter}}}, \quad (35)$$

into a rotational, a divergent, and two mixed rotational-divergent components. The rotational component represents the Orr mechanism as it is the sole energy source for 2D planar perturbations. The divergent component typically has the opposite effect on the energy evolution, yielding energy growth (decay) when the perturbations lean with (against) the shear. The first mixed rotational-divergent term represents the lift-up mechanism as it is the sole energy source for streamwise independent perturbations. The second mixed term (referred to as an interference term by Bakas [35]) is typically subdominant.

The evolution of the optimally growing perturbation with $K = 5$ and $\theta = 59^\circ$ is shown in Fig. 9, where its initial structure and its evolved structure at T_{opt} are illustrated [see Figs. 9(a) and 9(b),

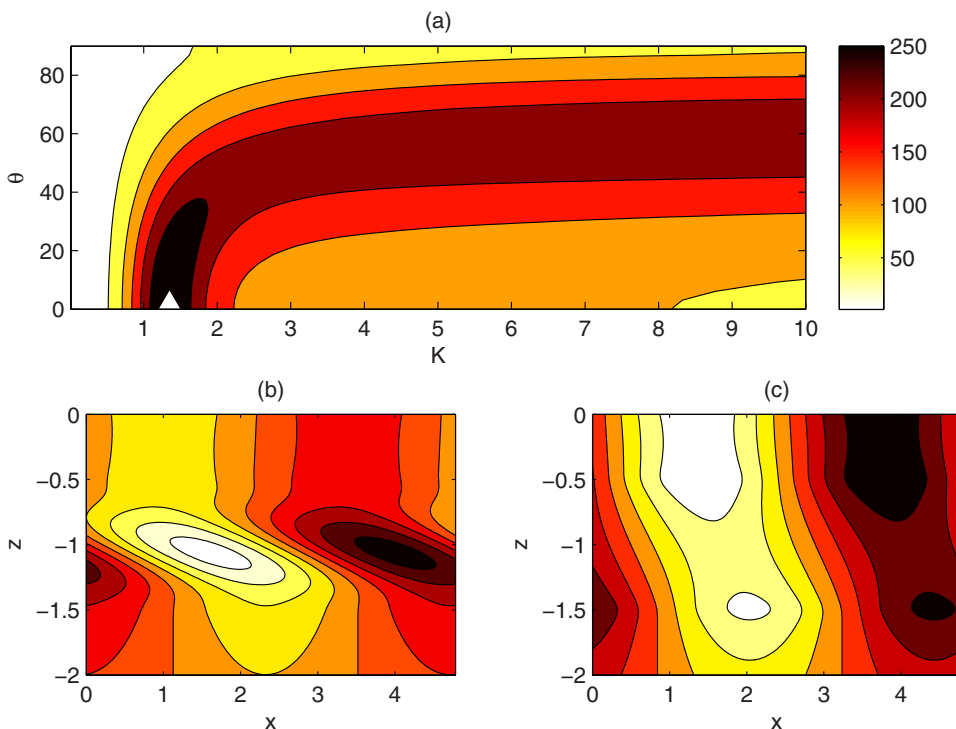


FIG. 10. (a) Optimal energy growth $G(T_{\text{opt}})$ as a function of horizontal wave number K and wave-number angle θ . (b) Vertical structure for the optimal perturbation with $K = 1.35$ and $\theta = 0^\circ$ marked by the triangle in (a) producing the maximum optimal growth G_{max} . Shown are contours of vertical velocity. (c) Structure of the exponentially unstable mode with $K = 1.35$ and $\theta = 0^\circ$. Shown are contours of vertical velocity. For all panels the optimization time is $T_{\text{opt}} = 10$, the Froude number is $F = 3$, and $\alpha = 1$.

respectively] along with the contribution of the three velocity components in the energy growth [see Fig. 9(c)] and the evolution of the four components of the Reynolds stress [see Fig. 9(d)]. As the perturbation leans initially against the shear, there is an initial growth of vertical velocity w [see Fig. 9(c)] due to the Orr component [see Fig. 9(d)] that reaches a maximum right before the phase lines in the x - z plane become vertical at $t \simeq 8$. As the perturbation continues to shear over and leans with the shear, the spanwise vorticity and the divergence become out of phase [see Fig. 9(b)] and the lift-up component of the Reynolds stress offsets the energy decrease caused by the Orr component and leads to an increase of the horizontal velocity components u and v [see Fig. 9(c)] in agreement with the findings of Vitoshkin *et al.* [32]. Since the horizontal velocity increase is much larger than the vertical velocity increase (the potential energy growth is insignificant in this case and is not shown), we conclude that the non-normal energy growth in this case is confined in the shear layer producing large velocity streaks and we speculate that the nonlinear manifestation of this growth will be a turbulent collapse of the shear layer without a surface imprint. Similar results are obtained for Froude numbers in the range $F < 1.8$.

For larger Froude numbers, even though there is significant growth of small-scale oblique perturbations with $\theta \simeq 60^\circ$ as shown in Fig. 10(a), the largest optimal growth is achieved for planar perturbations ($\theta = 0^\circ$) with lower wave numbers mostly within the region of branch II instability. However, even in this case in which most of the growth is attributed to the exponentially growing normal modes, maximum energy growth occurs for $K \simeq 1.3$ and there is significant growth for a wide range of perturbations in the horizontal, while the fastest exponentially growing perturbation has $K \simeq 1$ and there is a shortwave cutoff at $K = 1.5$ for the modal instability. In addition, optimal

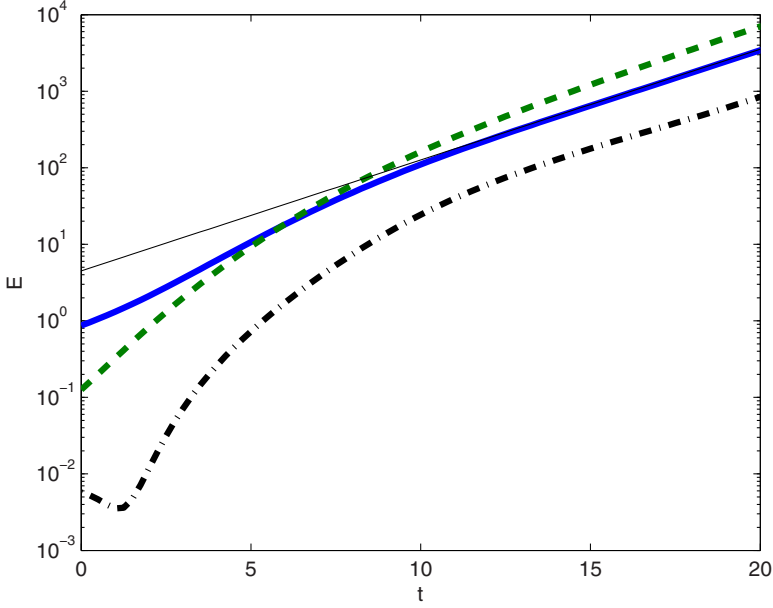


FIG. 11. Contributions of the horizontal components of velocity $\overline{E}_h = (1/2)\overline{u^2 + v^2}$ (solid line), vertical component of velocity $\overline{E}_w = (1/2)\overline{w^2}$ (dashed line), and potential energy $\overline{E}_{\text{pot}} = (1/2F^2)\overline{\eta^2}$ (dash-dotted line) in the total energy evolution for the optimal perturbation shown in Fig. 10(b). Exponential energy growth with the growth rate of the normal mode shown in Fig. 10(c) is also shown (thin line) for comparison.

growth is larger than the corresponding growth of the unstable normal mode by a factor of $O(10)$ (not shown). This excess growth is attributed to the energy amplification occurring in the time interval before phase locking of the edge waves occurs. To illustrate this consider the optimal initial perturbation with $K = 1.3$ and $\theta = 0^\circ$ shown in Fig. 10(b), which has phase lines tilted against the shear. As the perturbation is sheared over, it gains energy through the Orr mechanism that is the sole energy source for this 2D planar perturbation. This is illustrated in Fig. 11, plotting the contribution of the three velocity components and the potential energy in the energy growth. We observe that there is an initial energy boost with the amplitude of the vertical velocity increasing ten times within the first eight advective time units. Subsequently, the edge waves are excited and phase lock at $t \simeq 12$. The perturbation assumes the structure of the unstable normal mode shown in Fig. 10(c) and the energy grows exponentially at the growth rate of the unstable mode as shown in Fig. 11. As a result, the modal instability is excited with enhanced amplitude. A significant part of the energy growth is channeled into surface waves, as is evident by the large contribution of potential energy in the energy growth. We therefore expect a surface imprint of the instability and speculate that in the nonlinear regime this will lead to a concomitant collapse of the excited surface waves.

In order to investigate further the excitation of surface waves through non-normal growth of perturbations and whether there can be significant surface excitation for low Froude numbers as well, we calculate the initial perturbations of unit initial energy leading to the maximum potential energy growth. These optimal perturbations will therefore excite surface waves most effectively. The largest potential energy growth $G_{\text{pot}}(T_{\text{opt}})$ is given by the generalized eigenanalysis

$$\Phi_{\text{pot}}(T_{\text{opt}})\mathbf{v} = \mu_{\text{pot}}\mathbf{M}\mathbf{v}, \quad (36)$$

where $\Phi_{\text{pot}}(T_{\text{opt}}) = e^{A^\dagger T_{\text{opt}}}\mathbf{M}_{\text{pot}}e^{AT_{\text{opt}}}$ and \mathbf{M}_{pot} is the potential energy metric such that $(1/2F^2)\overline{\eta^2} = \mathbf{x}^\dagger\mathbf{M}_{\text{pot}}\mathbf{x}$. The optimal potential growth for $T_{\text{opt}} = 10$ is shown in Fig. 12(a) as a function of horizontal wave number K and wave-number angle θ . The perturbations producing the largest potential growth

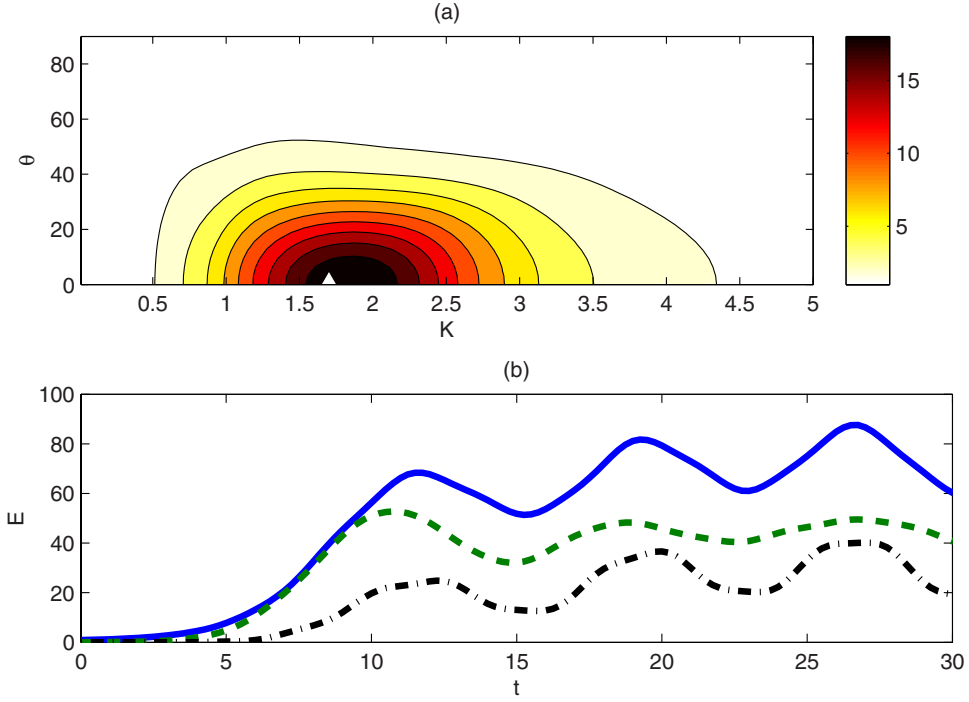


FIG. 12. (a) Optimal potential energy growth $G_{\text{pot}}(T_{\text{opt}})$ as a function of horizontal wave number K and wave-number angle θ . (b) Contributions of the horizontal components of velocity $\overline{E}_h = (1/2)\overline{u^2 + v^2}$ (solid line), vertical component of velocity $\overline{E}_w = (1/2)\overline{w^2}$ (dashed line), and potential energy $\overline{E}_{\text{pot}} = (1/2F^2)\overline{\eta^2}$ (dash-dotted line) in the total energy evolution for the optimal perturbation with $K = 1.7$ and $\theta = 0^\circ$ marked by the triangle in (a). For both panels the optimization time is $T_{\text{opt}} = 10$, the Froude number is $F = 1$, and $\alpha = 1$.

are planar ($\theta = 0^\circ$) and lead to a potential energy that is 18 times the initial perturbation energy. The reason is that vertical velocity in the shear layer and consequently at the surface is maximized through the Orr mechanism that is most effective for planar perturbations. It is also worth noting that, despite the fact that branch II unstable modes lead to significant potential energy growth, the perturbation leading to the maximum potential energy growth over a few advective time units has $K = 1.7$ and is modally stable. The energy evolution for the optimal perturbation with $K = 1.7$ and $\theta = 0^\circ$ is shown in Fig. 12(b). The initial energy amplification including the amplification of the vertical component of velocity leads to the excitation of surface waves with large amplitude as is evident by the large sustained potential energy.

The dependence of non-normal growth on the Froude number and on the shear is illustrated in Fig. 13, showing the maximum growth over all horizontal perturbations $G_{\text{max}} = \max_{K,\theta} G(T_{\text{opt}})$ as a function of Froude number for three values of the shear. For $\alpha = 1$ [see Fig. 13(a)], the maximum growth G_{max} is constant for $F < 1.8$. The reason is that the non-normal growth is produced by initial perturbations with small horizontal scales and a structure similar to the one shown in Fig. 9(a). These perturbations as discussed above produce large growth of horizontal velocities within the shear layer that has minimal imprint at the surface and is therefore independent of the gravitational acceleration. For larger Froude numbers the maximum growth G_{max} increases with F and asymptotes to about 340. This growth is achieved by planar perturbations with larger horizontal scales and a structure similar to the one shown in Fig. 10(b) instigating the modal instability as discussed above. For lower values of the shear [see Fig. 13(b)], modal instability is weak and small-scale 3D perturbations produce the maximum growth almost for all Froude numbers, whereas for larger values of the shear

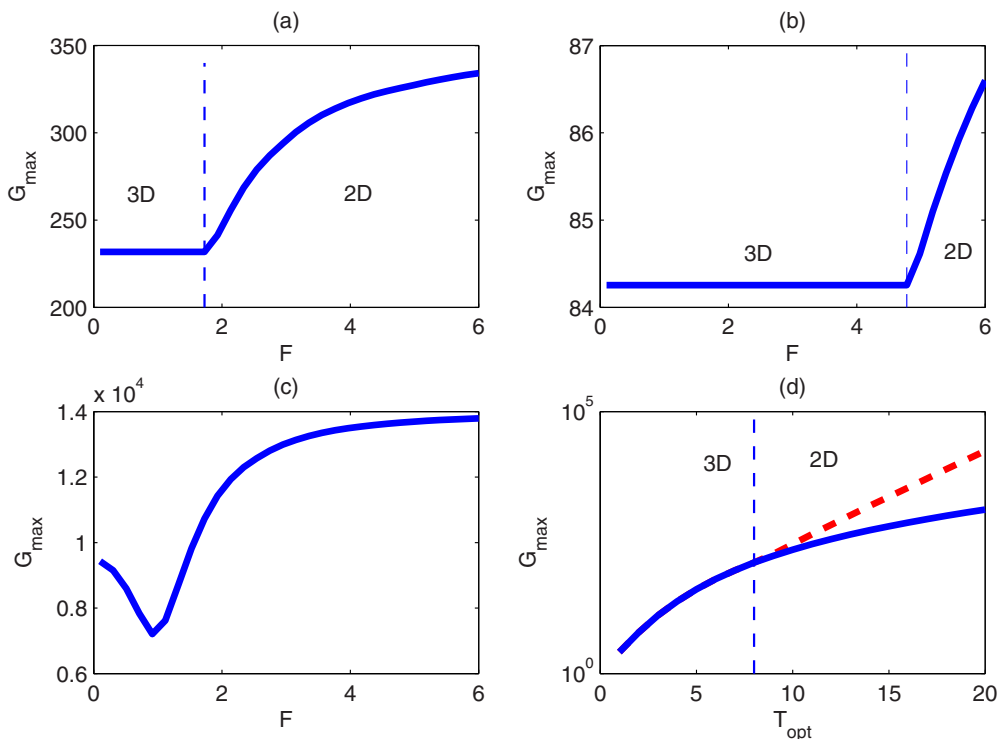


FIG. 13. Maximum value of the optimal growth G_{\max} over all perturbations as a function of the Froude number for (a) $\alpha = 1$, (b) $\alpha = 2/3$, and (c) $\alpha = 2$. The range where 3D and 2D perturbations produce the maximum growth in (a) and (b) is also indicated. The optimizing time is $T_{\text{opt}} = 10$. (d) Maximum value of the optimal growth G_{\max} over all perturbations as a function of T_{opt} for Froude number $F = 1$ (solid line) and $F = 3$ (dashed line). For $F = 1$ the optimal perturbations are three-dimensional, while for Froude number $F = 3$ the range where 3D and 2D perturbations produce the maximum growth is indicated. The shear is $\alpha = 1$.

[see Fig. 13(c)] larger-scale planar perturbations take advantage of the strong modal instability and excite the normal modes at large amplitude to produce explosive growth. Finally, we investigate the sensitivity of the obtained results on the optimization time T_{opt} . Figure 13(d) shows the maximum optimal growth G_{\max} as a function of T_{opt} for $F = 1$ and $F = 3$. We observe a monotonic increase of G_{\max} for both values of the Froude number, reaching very large values for large optimizing times. For $F = 1$, small-scale 3D perturbations produce this growth for all optimizing times, while for $F = 3$ the structure of the optimal perturbations changes. For $T_{\text{opt}} > 8$, the optimal perturbations are two dimensional and have large horizontal scales, while for small optimization times they are three dimensional and identical to the optimal perturbations for $F = 1$ (hence the identical growth achieved).

V. CONCLUSION

Modal and nonmodal growth of 3D perturbations in a shear flow with a free surface were investigated. Modal instability was explained in terms of the interactions between vorticity edge waves propagating at the two interfaces of vorticity discontinuity and surface gravity waves propagating at the interface of density discontinuity. The 3D vorticity and surface gravity edge waves interact by inducing velocities at the other waves' interfaces that modify the other waves' amplitudes and phase speeds and the resulting phase-locked configuration corresponds to the normal modes of the shear flow. The growth rates of the unstable modes were found to depend on two factors.

The first is the strength of the interaction of the edge waves, which is exponentially decreasing with the horizontal wave number $K = \sqrt{k^2 + l^2}$ of the plane-wave perturbations and decreasing with the angle $\theta = \arctan(l/k)$ that the phase lines of the plane-wave perturbations form with the spanwise direction. The second is the configuration (phase differences between the edge waves and amplitudes of the edge waves) at the phase-locked state as certain phase differences promote larger mutual amplitude growth of the edge waves.

The two branches of instability of Triantafyllou and Dimas [4] were recovered for 3D perturbations. The large-scale unstable modes in branch I that produce the largest growth rate for small Froude numbers result mainly from the interaction between the two vorticity edge waves while the surface wave has a stabilizing effect. The smaller-scale unstable modes in branch II that produce the largest growth rates for larger Froude numbers result mainly from the interaction between the surface and the lower vorticity edge waves with the upper vorticity edge wave enhancing the instability. For both branches, 2D perturbations in the x - z plane were found to have the highest growth rate consistent with Squire's theorem. For unstable modes in branch I, the main reason was found to be the decrease of the strength of the edge-wave interaction with the angle θ , while for the unstable modes in branch II the main reason was found to be the fact that 3D edge waves phase lock in a configuration that favors mutual amplitude growth less than the planar 2D edge waves. However, the range of unstable wave numbers is larger for oblique 3D perturbations as 3D edge waves with a wider range of scales are able to phase lock in a growing configuration.

Investigation of the nonmodal growth of 3D perturbations revealed large transient energy growth that increases with the Froude number. For low Froude numbers or low values of shear, 3D small-scale perturbations were found to produce the largest growth despite the fact that the prevalent exponentially growing perturbations are two dimensional and have larger scales. The growth is achieved through a synergy between the Orr and the lift-up mechanisms that was found to produce large streamwise streaks in the shear layer with no significant influence on the free surface. Surface waves can be excited by larger-scale planar perturbations utilizing the Orr mechanism to produce large vertical velocities, however the overall growth is suboptimal.

For large Froude numbers or large values of the shear, large-scale 2D perturbations were found to produce the largest energy growth. The perturbations with scales within the range of branch II instability were found to produce the largest energy growth, but comparable growth was found for perturbations with scales outside the branch II instability range. The optimal perturbations were found in this case to initially tilt against the shear and to grow due to the Orr mechanism, exciting the unstable mode with increased amplitude. A large part of the energy growth in this case is in vertical velocity and potential energy and as a result we expect the excitation of surface waves with significant amplitude. Since the inclusion of surface tension [9] and non-Boussinesq effects [36] influence the modal instability, an interesting avenue of future research would be the investigation of the influence of these effects in nonmodal growth of perturbations.

ACKNOWLEDGMENT

N.A.B. was supported by the AXA Research Fund.

-
- [1] D. H. Peregrine and G. P. Thomas, Finite-amplitude deep-water waves on currents, *Philos. Trans. R. Soc. London Ser. A* **292**, 371 (1979).
 - [2] M. S. Longuet-Higgins, Shear instability in spilling breakers, *Proc. R. Soc. London A* **446**, 399 (1994).
 - [3] J. H. Duncan, Spilling breakers, *Annu. Rev. Fluid Mech.* **33**, 519 (2001).
 - [4] G. S. Triantafyllou and A. A. Dimas, Interaction of two-dimensional separated flows with a free surface at low Froude numbers, *Phys. Fluids A* **1**, 1813 (1989).
 - [5] M. E. Stern and Y. A. Adam, Capillary waves generated by a shear current in water, *Mem. Soc. R. Liege* **6**, 179 (1973).

- [6] K. Itoh, H. Nakamura, H. Kumamaru, and Y. Kukita, Internal shear mode instabilities on high speed liquid jet, *J. Nucl. Sci. Technol.* **41**, 802 (2004).
- [7] E. A. Caponp, H. C. Yuen, F. A. Milinazzo, and P. G. Saffman, Water-wave instability induced by a drift layer, *J. Fluid Mech.* **222**, 207 (1991).
- [8] N. A. Bakas and B. F. Ioannou, Modal and nonmodal growth of inviscid planar perturbations in shear flows with a free surface, *Phys. Fluids* **21**, 024102 (2009).
- [9] M. S. Longuet-Higgins, Instabilities of a horizontal shear flow with a free surface, *J. Fluid Mech.* **364**, 147 (1998).
- [10] E. Heifetz, C. H. Bishop, and P. Alpert, Counter-propagating Rossby waves in the barotropic Rayleigh model of shear instability, *Q. J. R. Meteor. Soc.* **125**, 2835 (1999).
- [11] N. Harnik and E. Heifetz, Relating over-reflection and wave geometry to the counter propagating Rossby wave perspective: Toward a deeper mechanistic understanding of shear instability, *J. Atmos. Sci.* **64**, 2238 (2007).
- [12] A. Guha and G. A. Lawrence, A wave interaction approach to studying non-modal homogeneous and stratified shear instabilities, *J. Fluid Mech.* **755**, 336 (2014).
- [13] G. I. Taylor, Effect of variation in density on the stability of superposed streams of fluid, *Proc. R. Soc. London Ser. A* **132**, 499 (1931).
- [14] S. Goldstein, On the stability of superposed streams of fluid of different densities, *Proc. R. Soc. London Ser. A* **132**, 524 (1931).
- [15] F. P. Bretherton, Baroclinic instability and the short wave cut-off in terms of potential vorticity, *Q. J. R. Meteor. Soc.* **92**, 335 (1966).
- [16] V. V. Mikhailenko, H. J. Lee, and V. S. Mikhailenko, Non-modal analysis of the diocotron instability: Plane geometry, *Phys. Plasmas* **19**, 082112 (2012).
- [17] V. V. Mikhailenko, H. J. Lee, V. S. Mikhailenko, and N. A. Azarenkov, Non-modal analysis of the diocotron instability: Cylindrical geometry, *Phys. Plasmas* **20**, 042101 (2013).
- [18] B. F. Farrell and P. J. Ioannou, Generalized stability theory. Part I: Autonomous operators, *J. Atmos. Sci.* **53**, 2025 (1996).
- [19] P. J. Schmid and D. S. Henningson, *Stability and Transition in Shear Flows* (Springer, Berlin, 2001).
- [20] A. I. Smolyakov, P. H. Diamond, and V. I. Shevchenko, On the stability of three-dimensional disturbances of viscous flow between parallel walls, *Proc. R. Soc. London Ser. A* **142**, 621 (1933).
- [21] K. M. Butler and B. F. Farrell, Three-dimensional optimal perturbations in viscous shear flow, *Phys. Fluids A* **4**, 1637 (1992).
- [22] S. C. Reddy and D. S. Henningson, Energy growth in viscous channel flows, *J. Fluid. Mech.* **252**, 209 (1993).
- [23] B. F. Farrell and P. J. Ioannou, Optimal excitation of three-dimensional perturbations in viscous constant shear flow, *Phys. Fluids A* **5**, 1390 (1993).
- [24] T. Ellingsen and E. Palm, Stability of linear flow, *Phys. Fluids* **18**, 487 (1975).
- [25] M. T. Landhal, A note on an algebraic instability of inviscid parallel shear flows, *J. Fluid Mech.* **98**, 243 (1980).
- [26] T. D. Drivas and S. Wunsch, Triad resonance between gravity and vorticity waves in vertical shear, *Ocean Model.* **103**, 87 (2016).
- [27] E. Heifetz and J. Methven, Relating optimal growth to counterpropagating Rossby waves in shear instability, *Phys. Fluids* **17**, 064107 (2005).
- [28] U. Schaffinger, A short note on Squire's theorem for interfacial instabilities in a stratified flow of two superposed fluids, *Fluid Dyn. Res.* **14**, 223 (1994).
- [29] G. Mamatsashvili, G. Khujadze, G. Chagelishvili, S. Dong, J. Jimenez, and H. Foyi, Dynamics of homogeneous shear turbulence: A key role of the nonlinear transverse cascade in the bypass concept, *Phys. Rev. E* **94**, 023111 (2016).
- [30] W. M. F. Orr, The stability or instability of the steady motions of a perfect liquid and of a viscous liquid, *Proc. R. Irish Acad. Ser. A* **27**, 9 (1907), <http://www.jstor.org/stable/20490590>.

- [31] G. D. Chagelishvili, J. N. Hau, G. R. Khujadze, and M. Oberlack, Mechanical picture of the linear transient growth of vortical perturbations in incompressible smooth shear flows, [Phys. Rev. Fluids](#) **1**, 043603 (2016).
- [32] H. Vitoshkin, E. Heifetz, A. Y. Gelfgat, and N. Harnik, On the role of vortex stretching in energy optimal growth of three-dimensional perturbations on plane parallel shear flows, [J. Fluid Mech.](#) **707**, 369 (2012).
- [33] R. S. Lindzen and J. W. Barker, Instability and wave over-reflection in stably stratified shear flow, [J. Fluid Mech.](#) **151**, 189 (1985).
- [34] J. H. Duncan, V. Philomin, M. Behres, and J. Kimmel, The formation of spilling breaking water waves, [Phys. Fluids](#) **6**, 2558 (1994).
- [35] N. A. Bakas, Mechanisms underlying transient growth of planar perturbations in unbounded compressible shear flow, [J. Fluid Mech.](#) **639**, 479 (2009).
- [36] E. Heifetz and J. Mak, Stratified shear flow instabilities in the non-Boussinesq regime, [Phys. Fluids](#) **27**, 086601 (2015).